nature communications

Article

https://doi.org/10.1038/s41467-025-68158-6

Subnanoporous hydrophobic thin films for ultrahigh-efficiency seawater and brines desalination using membrane distillation

Received: 6 August 2024

Accepted: 15 December 2025

M. Obaid [1,7], Sofiane Soukane [1,7], Mohammed Rasool Qtaishat [2], Yaping Zhang [3], Vincent Guillerm [4], Hend Omar Mohamed[4], Maya Ayach [3], Venkatesh Singaravelu[3], Pedro Castaño [4], Guillaume Maurin [5], Mohamed Eddaoudi [4], Takeshi Matsuura[6] & Noreddine Ghaffour [1] ✉

Fabricating breakthrough materials capable of desalinating seawater and brine with high selectivity and low energy consumption is crucial for addressing global water and energy challenges. We report here the desalination capability of ultra-thin polymeric films with subnanometer pores synthesized through the polymerization of fluorinated trichlorosilane monomers and diamine-based monomers. The combination of subnanometer pore size, submicron thickness, and superhydrophobicity facilitates efficient liquid-to-vapor phase change in the membrane distillation process, enabling effective desalination performance. The thin-films demonstrate high salt rejection (99.8%), complete boron rejection, and water fluxes of 40 $L.m^{-2}.h^{-1}$ (1.88 $kWh.m^{-3}$, WRR_{sp} 0.32%) and 238 $L.m^{-2}.h^{-1}$ (20.65 $kWh.m^{-3}$, WRR_{sp} 3.87%) for seawater at 25 °C and 60 °C, respectively. For the desalination of real seawater reverse osmosis brine at 25 °C, the thin-films maintain 12 $L.m^{-2}.h^{-1}$ (4.4 $kWh.m^{-3}$, WRR_{sp} 0.09%) under comparable conditions. Their polymeric nature, chlorine resistance, and low energy requirements, indicate a potential for scalable and sustainable desalination systems.

Thin films have significantly contributed to membrane-based separation technologies in various fields, particularly seawater desalination[1], organic solvent separation[2], and crude oil separation[3]. They are typically fabricated by interfacial polymerization (IP)[4], molecular layer-by-layer[5], 3D-printing[6], and chemical vapor deposition[7] techniques. The IP strategy, based on the Schotten-Baumann reaction, is commonly employed for producing polymeric thin films, where the film grows at the interface of two immiscible phases via irreversible polymerization of two highly reactive multifunctional monomers[8–10]. The result is a self-terminated film growth with an overall thickness of a few hundred nm and a rough surface morphology[11]. In the early 1980's, Cadotte et al. developed the first thin film utilizing the IP technique, layering the thin film onto an ultrafiltration support to make a composite membrane (TFC). This led to a breakthrough with the development of membranes for reverse osmosis (RO), a desalination technology that dominates today's industry[12]. In a typical synthesis, aqueous solutions of organic amines react with organic solvents containing acyl chlorides, resulting in the formation of a thin and dense polyamide (PA) film. There have been several attempts to incorporate new features into the PA thin film in an effort to improve their performance[13–17]. Apart from its application in desalination, TFC has also been employed in the fractionation of crude oil or for molecular separation in organic liquids, commonly

---

[1] Biological and Environmental Science and Engineering Division, King Abdullah University of Science and Technology (KAUST), Thuwal, Saudi Arabia. [2] Chemical Engineering Department, School of Engineering, the University of Jordan, Amman, Jordan. [3] Core Laboratory, King Abdullah University of Science and Technology (KAUST), Thuwal, Saudi Arabia. [4] Physical Sciences and Engineering Division, King Abdullah University of Science and Technology (KAUST), Thuwal, Saudi Arabia. [5] ICGM, Université de Montpellier, Montpellier, France. [6] Chemical and Biological Engineering Department, University of Ottawa, 161 Louis Pasteur, Ottawa, ON, Canada. [7] These authors contributed equally: M. Obaid, Sofiane Soukane. ✉ e-mail: noreddine.ghaffour@kaust.edu.sa

referred to as organic solvent RO[18,19]. Hydrophobic thin films produced by either capping thin films with a hydrophobic group or directly incorporating the hydrophobic group into the monomers during the reaction, demonstrated remarkably fast liquid transport[20,21]. On one hand, the hydrophobic vesicles facilitate efficient paths for the transport of nonpolar liquids across the thin film[3]. On the other hand, the electrostatically negative fluorous inner surface of the hydrophobic nanochannels breaks water clusters, thus allowing more water to pass[22]. Also, the hydrophobic thin films perform excellently in the evaporation-based desalination process, which relies on the transport of water vapor through the hydrophobic nanopores[23–25]. In previous work, we also delivered evidence to support the hypothesis that a thin film of sub-micron thickness has promise for significantly improving the efficiency of desalination[26]. Therefore, the development of a superhydrophobic thin film with high permselectivity could be a breakthrough for sustainable desalination of highly saline brines. To address this challenge, herein we report the design of scalable superhydrophobic polymeric thin films with submicron thicknesses. The thin film grows in a minute at the organic/aqueous interface owing to the reaction between fluorinated trichlorosilane molecules and an m-phenylenediamine (MPD) monomer. The thickness of the thin films can be readily adjusted by controlling the fabrication conditions (i.e., reagent concentration and reaction time). As-synthesized superhydrophobic thin films are layered on a hydrophilic porous material for structural support and additional enhancement of water evaporation[27], taking advantage of the effect of a hydrophilicity gradient in the composite membrane design[25]. Using the membrane distillation (MD) process, the resulting thin films efficiently desalinate highly challenging solutions i.e., real RO desalination brine, real seawater, scale-forming ions, and monovalent ions, with the lowest energy consumption reported to date. We demonstrate, using a multiscale model, that the experimentally observed evaporation fluxes can be predicted over a wide range of operating conditions using the Kelvin equation with curvature-dependent water surface tension at the pore level[28], providing an important connection between the molecular behavior of water and the tangible performance of the designed membrane.

Results

Synthesis of polymeric thin films

We synthesized scalable polymeric thin films with various thicknesses (60.6 to 238.5 nm) for desalination using a straightforward, scalable, and controllable IP technique. This IP involves the reaction between 1H,1H,2H,2H-perfluorododecyltrichlorosilane (FTCS) and MPD at the interface of two immiscible solutions, forming a superhydrophobic thin film (Fig. 1a and Fig. S1). The freshly prepared FTCS/hexane (organic phase) solution was slowly poured into the MPD/deionized (DI) water (aqueous solution). Upon pouring the FTCS/hexane solution, the head (–$SiCl_3$) of FTCS gets closer to the water surface, whereas its hydrophobic tail remains in the organic phase. Once the FTCS/hexane solution spreads, the head group undergoes rapid hydrolysis and aminolysis reactions with water and MPD, respectively, followed by a condensation reaction (Fig. 1a–c), forming a free-standing superhydrophobic thin film with subnanometer pores at the aqueous–organic interface (Fig. S1a), that was then transferred onto a porous support. Further, we explored the effect of the IP reaction time and FTCS concentration on the thickness, physicochemical properties, and performance of the synthesized thin films (Supplementary Notes 1 and 2). For briefness, the thin-film samples are referred to as TFx–y, where x is the FTCS concentration (wt/vol%) and y is the IP reaction time (min), respectively (e.g., TF0.1–0.5; Table S1). The scalability is demonstrated by fabricating a free-standing thin film with an area of 324.0 cm^2 (18 cm×18 cm) (Fig. S1b), without compromising its mechanical strength. As such, owing to its robust mechanical integrity, the scaled-up free-standing thin film was safely transferred to the surface of a porous support (Fig. S1c). To support scalability, the thin film was also synthesized using the support-IP method[29].

Scanning electron microscopy (SEM) observations of the thin films transferred onto the substrate (substrate properties in Table S2) demonstrate the integrity of the thin films (Fig. 1d–h). The morphology of the thin films varied with the FTCS concentration and IP reaction time (Fig. S2). For a short IP reaction time (0.5 min), the thin film exhibited a smooth surface with small nodular features. As the reaction time increased (1–3 min), more prominent leaf-like structures developed, creating a distinct ridge-and-valley topography (Fig. 1d–g and Fig. S2). Increasing FTCS concentration further intensified these surface features, resulting in a denser distribution of leaf-like formations (Fig. S2i–l). The two-dimensional (2D) atomic force microscopy (AFM) images (Fig. 2a and Fig. S3) were consistent with the SEM observations. Cross-sectional SEM images of the thin films on 60 μm-thick substrates revealed film thicknesses ranging from 60.6 nm to 238.5 nm, demonstrating a direct correlation with longer IP reaction times and higher FTCS concentrations (Fig. 2b–f; and Fig. S4 and Table S3). AFM profiling of free-standing thin films, transferred onto silicon wafers, further confirmed that thicknesses remained below 250 nm, with a clear trend of increasing thickness with longer IP reaction times and elevated FTCS concentrations (Fig. 2g, h, Fig. S5). Additionally, surface roughness values varied with the IP reaction time or FTCS concentration (Fig. S6 and Table S3).

Structural insights provided by grazing incidence wide-angle X-ray scattering (GI-WAXS) provide further understanding of molecular orientation and arrangement within the films (Figs. S7 and S8). The in-plane GI-WAXS profiles of films TF0.1–1, TF0.2–1, and TF0.3–1 exhibit consistent peaks around $Q_{\|} = 1.27$ Å^{-1}, corresponding to a d-spacing of approximately 0.495 nm[30–32]. This uniform in-plane feature suggests a consistent molecular arrangement, such as π-π stacking of aromatic groups perpendicular to the supporting substrate, an arrangement likely established during the IP process[30,31,33]. In contrast, the out-of-plane GI-WAXS profiles exhibited distinct peak positions for each sample ($Q_{\perp} = 0.36$ Å^{-1}, 0.55 Å^{-1}, and 0.90 Å^{-1} for TF0.1–1, TF0.2–1, and TF0.3–1, respectively), corresponding to d-spacing of 1.748 nm, 1.142 nm, and 0.698 nm, respectively (Fig. 2i, j and Figs. S7 and S8). These variations reflect differences in molecular packing density along the out-of-plane direction, likely influenced by polymerization kinetics[33–39]. This anisotropic arrangement, characterized by consistent in-plane alignment and variable out-of-plane packing, suggests that thickness and cross-linking density may influence transport properties, as thicker films with higher structural density could resist vapor transport due to increased structural complexity.

The estimation of the thin film porosity based on the BET method yielded a value of 4.94% (Supplementary Notes 2.9 and 3.6). The thermal conductivity measurements of the polymeric thin films showed a value of 0.07 ± 0.02 $W.m^{-1}.K^{-1}$ (Fig. S9), highlighting their strong thermal insulation properties, a crucial factor for efficient desalination. The low thermal conductivity, coupled with controlled structural anisotropy, enables these films to minimize heat loss while allowing selective vapor transport. The chemical structure of the polymeric thin films was validated using Fourier-transform infrared (FTIR) and Raman spectroscopy (Supplementary Note 3.2). The band at 880 cm^{-1} is assigned to the Si–N stretching mode[40–43], confirming that FTCS reacted with MPD via an aminolysis reaction (Fig. 1b and Fig. S10), forming a continuous thin film (Fig. 1b). Additionally, the bands at 1068 cm^{-1} and 1024 cm^{-1} are assigned to the Si–O stretching mode of Si–O–Si (Fig. S10), resulting from hydrolysis and condensation of FTCS, respectively. We characterized the degree of cross-linking in the polymeric thin films by observing the relative intensities of Si–N and Si–O–Si peaks, normalized to an internal C–C reference (Supplementary Note 3.2). The increasing peak ratios, correlating with higher FTCS concentrations and extended reaction time, indicate more cross-linking as revealed in the growth of normalized Si–N and

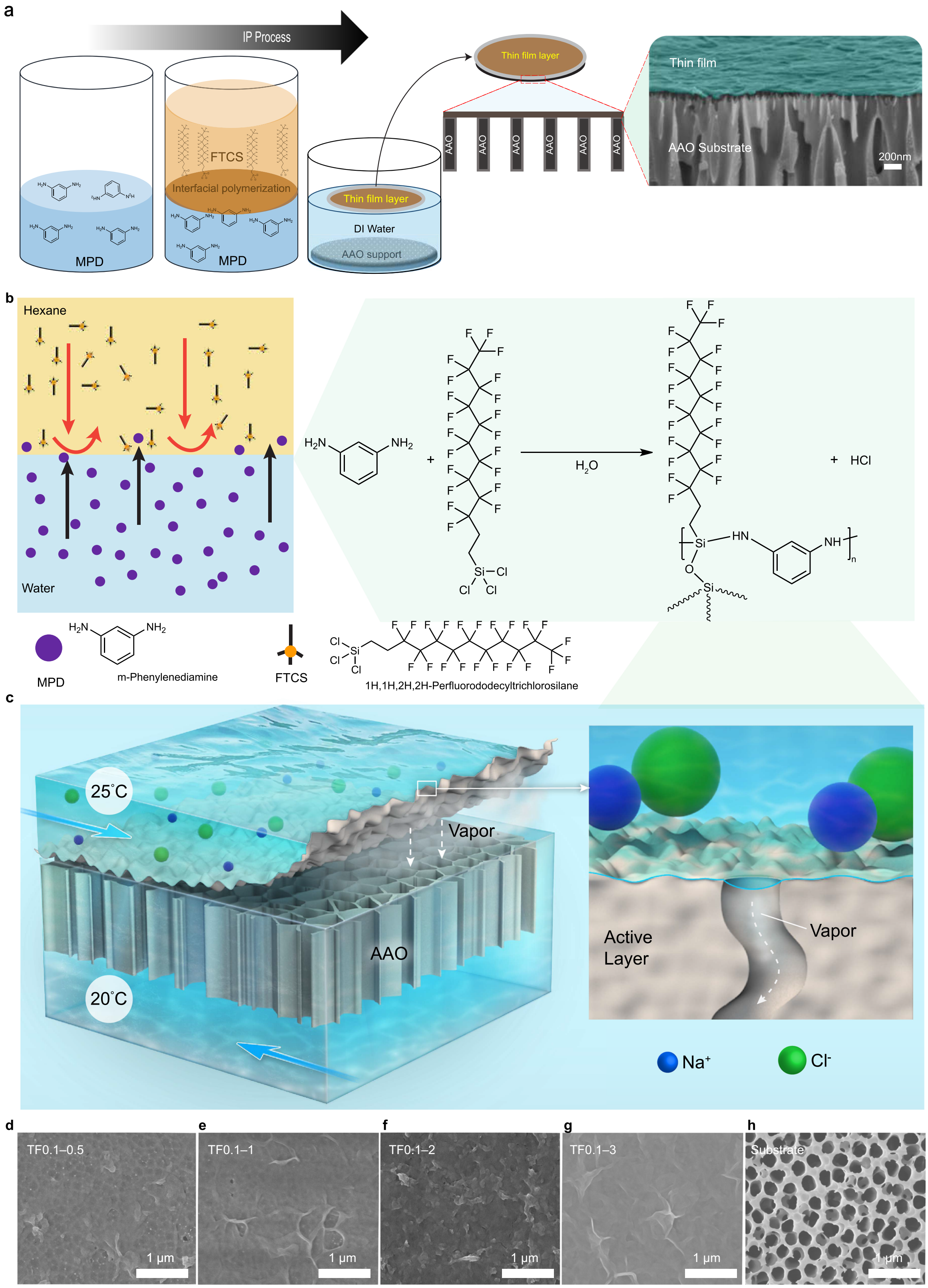

Fig. 1 | Interfacial polymerization synthesis and structural formation of the superhydrophobic thin film. a Schematic of the synthesis of a superhydrophobic polymeric thin film at the hexane–water interface, where m-phenylenediamine (MPD) is dissolved in deionized (DI) water, followed by pouring a 1H,1H,2H,2H-perfluorododecyltrichlorosilane (FTCS)/hexane solution to begin IP at the hexane-water interface. The resulting film is removed and transferred to the substrate to obtain the composite membrane. Scanning electron microscopy (SEM) cross-section of the polymeric thin film (TF0.2–1) supported by the substrate; scale bar = 200 nm. **b** Hypothetical mechanism of the IP reaction between MPD and FTCS. **c** A schematic of the thin film on the porous substrate. SEM surface images of the supported polymeric thin films fabricated at the IP reaction times of **d** 0.5, **e** 1, **f** 2, and **g** 3 min; MPD/DI water and FTCS/hexane concentrations were 3 and 0.1 wt/vol %, respectively. **h** SEM image of the porous support. Scale bar = 1 μm.

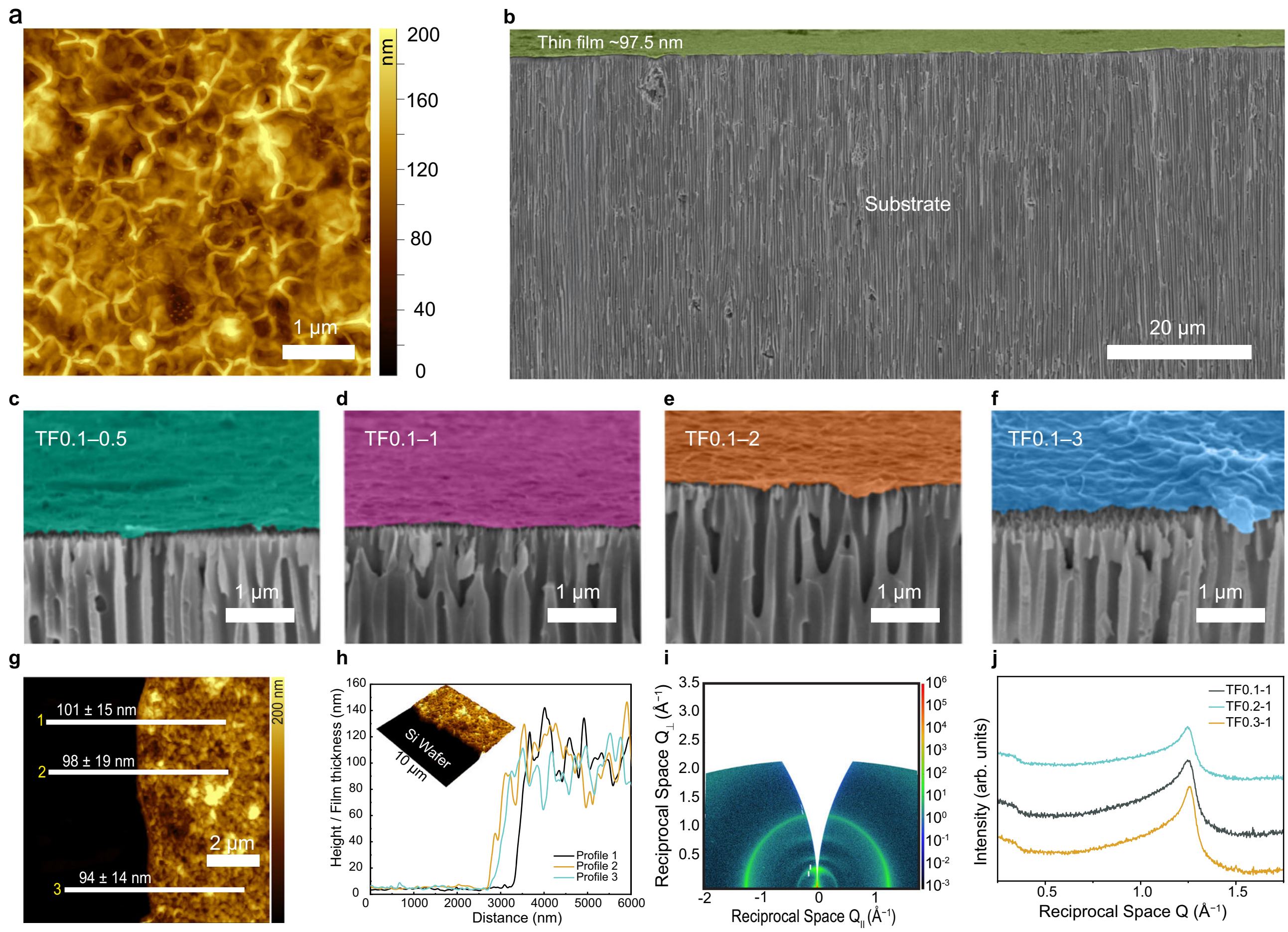

Fig. 2 | Multiscale morphological and crystallographic characterization of the polymeric thin film. a Atomic force microscopy (AFM) 2D image (scan area 5 × 5 μm) for TF0.1–1 transferred to the substrate; Scale bar = 1 μm. **b** Cross-sectional scanning electron microscopy (SEM) images of polymeric thin film TF0.1–1 supported on a ~60-μm-thick substrate; Scale bar = 20 μm. Effect of reaction time of **c** 0.5, **d** 1, **e** 2, and **f** 3 min on the cross-sectional morphology of the fabricated thin films prepared with an m-phenylenediamine (MPD) concentration of 3 wt./vol% and an 1H,1H,2H,2H-perfluorododecyltrichlorosilane (FTCS) concentration of 0.1 wt./vol%. Scale bar = 1 μm. **g** and **h** 3D AFM height image and height or thickness profile of a free-standing thin film transferred to a silicon wafer; Scale bar = 2 μm. **i** Wedge-corrected GI-WAXS images of the TF0.1–1 thin film, showing grazing incidence data along the out-of-plane component ($Q_\perp$) versus the in-plane component ($Q_{||}$). **j** One-dimensional scattering patterns and GI-WAXS images of the thin films (TF0.1–1, TF0.2–1, and TF0.3–1), In-plane scattering profile (Q | |), representing reciprocal space parallel to the thin surface.

Si–O–Si peaks, suggesting a dynamic interplay between aminolysis and condensation in forming the film structure (Fig. S10 and Table S4). Furthermore, Raman spectroscopy supported the FTIR results (Figs. S10 and S11). Complementing the FTIR findings, Energy Dispersive X-ray (EDX) analysis was conducted to further evaluate the chemical composition and stoichiometry. The analysis of the Si to N ratios (elements unique to FTCS and MPD, respectively) confirmed that the FTCS concentration plays a pivotal role in the film composition. The results from these analytical techniques demonstrate the relationship between monomer concentration and the resulting structure of the polymeric thin film (Table S5). Based on these results, the reaction mechanism can be explained as follows: when the FTCS/hexane solution is added to the MPD/DI water solution, highly active $-SiCl_3$ groups are hydrolyzed by water, forming –Si–OH, whereas others react with MPD to form –Si–NH and release HCl as a byproduct, as illustrated in Fig. S12.

Fluorine-based chains on the thin-film surface could produce low surface energy, imparting superhydrophobicity with water contact angle (WCA) values > 160°. Moreover, varying the IP reaction time or FTCS concentration had a negligible effect on the wettability of the thin films (Fig. S14a and Table S2). Importantly, the thin films exhibited superhydrophobicity toward salty water (30 $g.L^{-1}$ of NaCl) over a wide range of pH values (1.5–12.0) and toward a surfactant-stabilized oil-in-water emulsion (Fig. S14b). As a comparison, the commercial hydrophobic membranes (with different porosities of 39.6% ± 4.7% (Commercial#1) and 48.3% ± 4.3% (Commercial#2) exhibited WCA values < 135°, smaller than those of the fabricated thin films (Supplementary Note 1.1 and Table S2).

Desalination performance

Before performing desalination experiments, the as-synthesized thin films were transferred onto a commercial hydrophilic substrate. The performance of the thin films was evaluated for the desalination of saline water with different concentrations in terms of water-vapor flux and salt rejection using membrane distillation (MD) process. These membranes were sandwiched between the feed (saline solution) and distillate (DI water) streams, with the thin film facing the feed solution (Fig. S15). To provide a slight driving force across the membrane, we set the transmembrane temperature difference at a very low value of 5 °C, using a low feed temperature of 25 °C and a distillate temperature of 20 °C.

The vapor flux was notably influenced by the concentration of FTCS, decreasing with higher concentrations, while the impact of IP reaction time was less pronounced (Fig. 3a). As such, despite increased

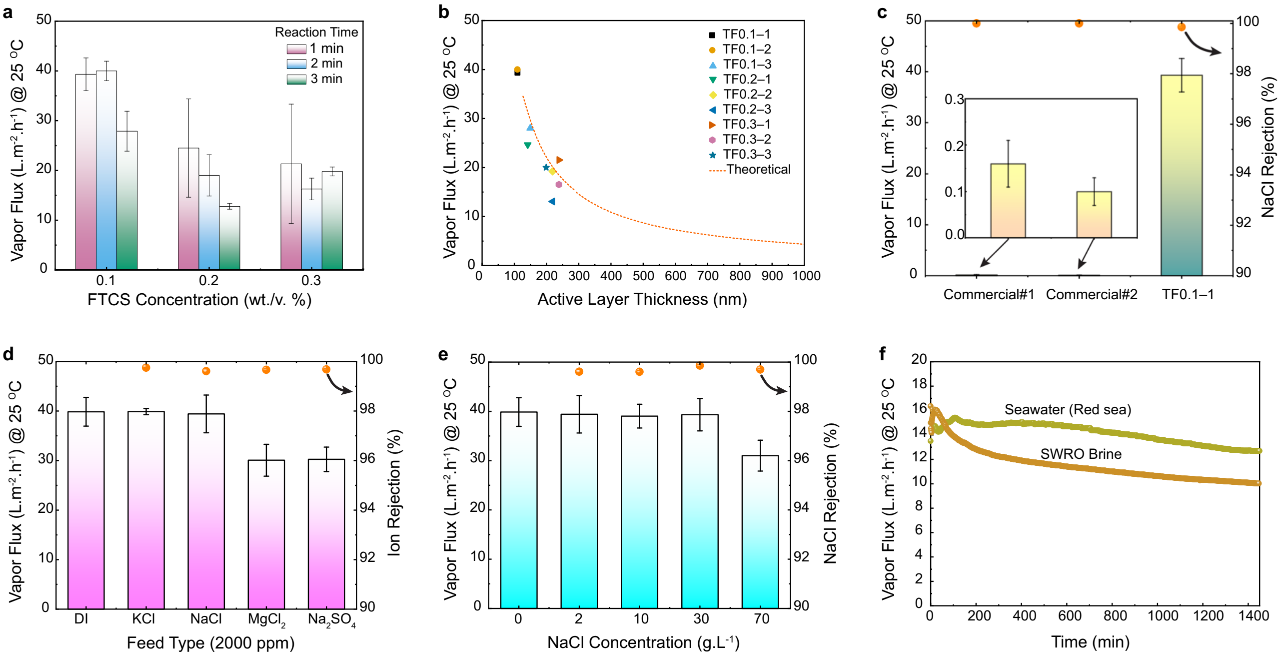

Fig. 3 | Desalination performance of the supported polymeric thin-film membranes. a Effect of the 1H,1H,2H,2H-perfluorododecyltrichlorosilane (FTCS) concentration and reaction time on the desalination performance of the polymeric thin films using the 30 g.L^{-1} of NaCl aqueous solution as the feed. **b** Vapor flux as a function of thin-film thickness for a feed temperature of 25 °C. The dotted orange line represents the vapor flux predicted by the Beskok and Karniadakis unified mass transfer model, and the symbols represent the experimental results. **c** Average experimental flux and salt rejection of the TF0.1–1 membrane and commercial membranes for desalination, with commercial membranes showing almost zero flux. The inset provides a detailed zoom on the flux of commercial membranes. **d** Water-vapor flux and ion rejection of the TF0.1–1 thin film in treating salt solutions with different ions. **e** Effect of feed salinity on the desalination performance of the TF0.1–1 thin film in terms of vapor flux and salt rejection. The desalination conditions were a saline feed at 25 °C and a distillate at 20 °C. **f** Long-term operation of the TF0.1–1 thin film showing stability towards desalination of real seawater (Red Sea) and real SWRO brine. Error bars represent the standard deviation of five independent experiments, and central values denote the mean measurements.

roughness, which typically enhances flux by increasing surface area, a decline in vapor flux was observed with higher FTCS concentrations or extended reaction times (Table S3). This decline can be attributed to a corresponding increase in film thickness (Fig. 3b) and tighter molecular packing, as evidenced by GI-WAXS out-of-plane profiles (Figs. S7 and S8). Specifically, the d-spacing for TF0.1–1 was approximately 2.5 times greater than for TF0.3–1, reflecting increased compact molecular packing[34–36]. The decrease in d-spacing and increase in film thickness indicated that higher concentrations promote additional polymer growth and denser molecular packing along the out-of-plane direction (Figs. S7 and S8 and Table S3). The tighter molecular packing and increased cross-linking density observed in thicker films are likely to contribute to increased transport resistance, reducing flux. For example, at a 1-minute reaction time, increasing the FTCS concentration from 0.1% to 0.3% resulted in a substantial thickness increase from 97.5 nm to 238.5 nm (Fig. 3b and Table S3). These structural and morphological variations underscore the trade-off between surface roughness, thickness, and molecular packing, explaining why the thinner, smoother membrane (TF0.1-1) achieved the best performance.

The best-performing thin film, TF0.1–1 (0.1 wt.% FTCS, 1 min reaction time), achieved a vapor flux of 40 ± 3 L.m^{-2}.h^{-1} and salt rejection of ~99.9% for simulated seawater (30 g.L^{-1} NaCl), significantly outperforming commercial membranes (Commercial#1 and Commercial#2), which showed almost zero flux under the same conditions (Fig. 3c). The obtained flux is more than double the RO flux reported for treating seawater with a hydraulic pressure of 55 bar[44]. Furthermore, the TF0.1–1 efficiently removed both monovalent (K^+, Na^+, and Cl^-) and divalent (Mg^{2+} and SO_4^{2-}) ions from water with a high separation efficiency of 99.9% (Fig. 3d). However, the flux slightly decreased when divalent ions were used, which could be attributed to the magnesium and sulfate ion scaling and different water activities associated with multivalent ions[45]. Additionally, the excellent desalination performance of TF0.1–1 was sustained at different NaCl concentrations (Fig. 3e), even when the concentration of the salt in the feed was increased to 70 g.L^{-1} (brine; 31 ± 3 L.m^{-2}.h^{-1}), which cannot be achieved using RO. Interestingly, the as-prepared thin film (TF0.1-1) exhibits excellent performance towards real seawater (Red Sea salinity = 40.98 g/L, Table S6) and real desalination brine (discharge from SWRO commercial plant = 74.4 g/L, Table S6) with average permeate fluxes of 14 ± 1 and 12 ± 1 L.m^{-2}.h^{-1} and high salt rejections of 99.3 ± 0.3 and 99.0 ± 0.6 %, respectively (Fig. 3f) at a feed temperature of 25 °C and atmospheric pressure. Importantly, while our group reported the evidence of boron volatility (ppb level) in MD starting at about 60 °C, this thin film acts as a full barrier to boron (100% rejection in all cases)[46]. Furthermore, after the long-term desalination of real feeds, the SEM analysis (Fig. S16a,b) of the used thin films revealed that the morphology remains stable even at high cross-flow velocities, demonstrating its superior mechanical integrity. Moreover, the films showed high resistance to chlorine (Fig. S16c), which further enhances stability. This excellent long-term stability in treating real seawater and real SWRO brine (Fig. 3f) and the fabrication of large samples of 324.0 cm^2 (Fig. S1b) demonstrate the possibility of scaling up the composite membrane manufacturing process.

We investigated all synthesized thin films over a wide range of feed temperatures (25 °C–60 °C), covering waste heat generated from industrial plants as low-grade heat sources. For all thin films, the vapor flux increased with an increase in feed temperature due to an increase in driving force (vapor-pressure difference; Fig. 4a and Figs. S17 and S18). In addition, Fig. 4a reveals that the TF0.1–1 membrane provided an ultrahigh vapor flux (238.2 ± 17.5 L.m^{-2}.h^{-1}), six times higher than that of the commercial membranes (41 ± 1 and

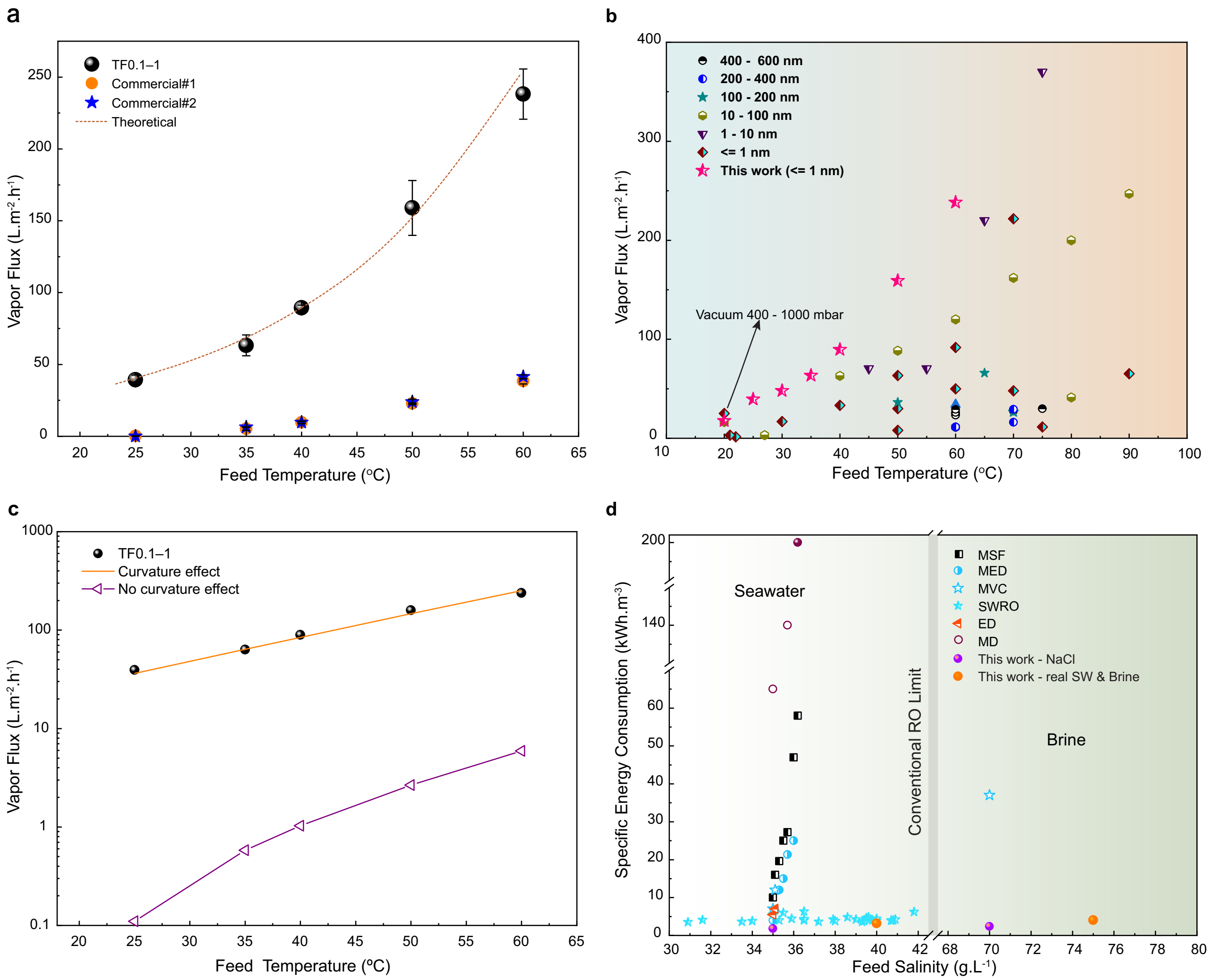

Fig. 4 | Temperature-driven desalination performance and energy metrics of the polymeric thin-film membrane. **a** Average water flux versus the transmembrane temperature difference (feed temperature of 25–60 °C and distillate temperature of 20 °C) for the TF0.1–1 and commercial polytetrafluoroethylene membranes. The symbols denote the experimental results, and the dotted orange line denotes the results of the Beskok and Karniadakis (BK) unified model. **b** Desalination performance comparison of the TF0.1–1 thin film (feed temperature from 25–60 °C) with commercial and literature-reported membranes (detailed conditions in Tabs. S7 and S8). **c** Vapor flux determined using the BK unified model as a function of feed temperature with and without vapor-pressure enhancement caused by the thin film with nanosized pores (feed and distillate temperatures set to 25 and 20 °C, respectively). **a**–**c** The feed solution used was 35 g.L^{-1} NaCl at a flow rate of 500 mL.min^{-1}. Error bars represent the standard deviation of five independent experiments, and central values denote the mean. **d** Comparison between SEC of TF0.1–1 and reported SEC required to desalinate feeds with different salinity using various desalination technologies (MSF: multistage flash distillation, MED: multi-effect distillation, MVC: mechanical vapor compression, SWRO: seawater reverse osmosis, ED: electrodialysis, MD: membrane distillation).

38 ± 2 L.m^{-2}.h^{-1}) at a transmembrane temperature difference of 40 °C (feed at 60 °C and distillate at 20 °C). Moreover, the flux exhibited by the TF0.1–1 membrane is higher than that reported for other commercial membranes in the literature (Table S7). Additionally, this desalination flux (at a 60 °C feed temperature) is among the highest values reported in the literature for polymeric and inorganic membranes (Fig. 4b). A TF0.1–1 had higher fluxes than other advanced materials with subnanometer pores, including graphene (226.6 L.m^{-2}.h^{-1} at 70 °C under −800 mbar vacuum)[23], nanoporous carbon (221.6 L.m^{-2}.h^{-1} at 90 °C and under −825 mbar, VMD mode)[24], and COFs (220.0 L.m^{-2}.h^{-1} at 65 °C and under −160 mbar, VMD mode)[25]. However, the performance of these materials was assessed under vacuum and higher temperatures, requiring additional energy (Fig. 4b and Table S8). Additionally, all thin films exhibited high salt rejection (>99.0%) due to their superhydrophobicity, which prevented liquid penetration (Fig. S18).

Desalination mechanism

The high vapor flux produced by the thin films could be attributed to several factors. First, vapor-pressure enhancement due to the curved meniscus at the entrance of the superhydrophobic subnanometer pores of the thin film results in a substantial increase in the evaporation driving force. This effect is facilitated by the thin film's low thickness and the hydrophobicity gradient provided by the hydrophilic support. By performing additional experiments, we confirmed the hypothesis that the finely tuned properties of the thin film, such as the lower thickness and a lesser degree of cross-linking, represent the main contribution to the high vapor flux. The original hydrophilic substrate and modified hydrophobic substrate (pore size = 0.2 µm) were evaluated in the same desalination system at a high feed temperature of 60 °C. As presented in Fig. S19, the hydrophilic support demonstrated no salt rejection due to its hydrophilicity, as expected. In addition, the modified hydrophobic support produced a very low vapor flux value of

16.8 ± 2 L.m^{-2}.h^{-1} and 99.99% salt rejection (feed at 60 °C and distillate at 20 °C). However, the membrane did not produce any flux at 25 °C inlet feed. The poor performance of the hydrophobic support confirms that the fabricated thin film is the key to the experimentally observed high desalination performance. Recent molecular dynamics simulations and experimental studies have indicated that the water evaporation flux in nanopores is orders of magnitude higher than that of bulk water evaporation. In addition, the evaporation rate is significantly increased by reducing the confinement characteristic size[47,48], which could be useful in designing efficient materials for low-energy desalination processes. Molecular dynamics simulations, conducted at 27 °C and low pressure (≤ 1 atm), revealed that water exists in a vapor-like state in hydrophobic subnanometer carbon nanotubes (0.8–1.0 nm)[49] and between hydrophobic nanoscale sheets ($d \leq 0.5$ nm)[50], owing to the peculiar behavior of water under confinement effects[51,52].

We further performed an analytical and numerical investigation of transmembrane mass transfer to provide a physical basis for the high vapor fluxes observed using the as-prepared thin films under ambient operating conditions (detailed explanations are provided in Supplementary Note 6). Because the developed thin films have a submicron thickness and subnanometer pores, we used the Beskok and Karniadakis[53] (BK) unified model to determine the mass transfer across these thin films. This unified model is based on the solution of momentum equations using a second-order slip boundary condition to account for the gas slippage and rarefaction effects observed in narrow channels of microstructures[54]. This approach has been successfully used to describe gas transport in porous media[55,56] and nanopores[57,58]. The transmembrane mass-transfer model was embedded in a computational fluid dynamics (CFD) code to account for the entire desalination system used in these experiments, including the feed and distillate channels. This implementation enables the prediction of momentum, heat, and mass transfer in both channels, coupled in a conjugate approach with heat and mass transfer across the thin film[59,60]. The heat transfer across the membrane includes the conduction across the membrane-air-water vapor composite structure as well as the latent heat transferred with the vapor convection from the feed to the permeate side of the membrane. Additionally, the heat extracted from the feed and added to the permeate as water evaporates and condensates, respectively, is taken into account in the calculations (see equations in Supplementary Note 6). Computations were performed to estimate the theoretical water-vapor flux, in which the effect of vapor-pressure enhancement (water evaporation in hydrophobic nanopores) was considered using the Kelvin equation, which remains valid in nanometer confinements (Fig. S20)[61,62]. It is worth noting that the Knudsen - Molecular - Poiseuille Transition (KMPT) model, which is a widely used model to describe mass transfer in MD, was not able to reproduce the permeate flux evolution with temperature (see Fig. S21). Given the subnanometer pore size of the prepared membrane, the KMPT model reduces to diffusion, which is less sensitive to temperature changes compared to Poiseuille flow[63]. On the contrary, the BK model, which retains features of the Poiseuille flow while compensating for the damping of the small pore radius with the rarefaction coefficient, is able to reflect the flux changes with temperature at high Knudsen numbers.

The theoretical results revealed that the vapor flux enhanced by subnanometer pores is considerably higher than the vapor flux produced by common microporous membranes (Fig. 4b, c). The vapor-pressure enhancement occurs primarily on the feed side due to the submicron thickness and subnanometer pores. Indeed, as the moderate flow pressure pushes water at the feed–thin film interface, an increase in local vapor pressure occurs, whereas it remains almost unchanged at the meniscus of the substrate pores because of the larger pore size (~0.2 μm; Fig. 4c).

Moreover, the submicron thickness and the very low thermal conductivity of the thin-film layer play an important role in enhancing the vapor flux by maximizing the driving force across the membrane[64]. The simulation results reported in Fig. 3b indicate the drastic effect of the thin-film thickness on the vapor fluxes for a feed temperature of 25 °C and a distillate temperature of 20 °C. If the thin-film thickness is increased from 120 nm to 1 μm, which is still considerably thinner than traditional membranes, the water flux decreases by a factor of eight, due to an increase of the mass transfer resistance. The permeate fluxes obtained using the BK model for different thicknesses of the thin films are similar to those in the experimental results (Fig. 3b). Interestingly, in Fig. 3b, there is no apparent optimum in the range of film thicknesses that were fabricated, as the permeate flux keeps increasing with thinner films. Therefore, with an ultrafast vapor transport, a film thickness two orders of magnitude thinner and pore size two to three orders of magnitude smaller than those of common MD membranes, the optimum film thickness below which conduction losses start penalizing the processes has shifted below 60 nm. This is further consolidated with Fig. 4a which demonstrates that the results using the BK model with varying temperatures are aligned with the experimental results (corresponding to the properties of TF0.1–1). The unified model can reproduce the trend of the permeate flux variations, probably due to its calibration at a high Knudsen number using both experiments and simulations[53] and its embedding in a fully coupled approach, thus ensuring proper heat and mass transfer from the feed to the permeate domains.

Energy saving

Energy consumption remains a major contributor to the total cost of desalination, making energy efficiency a critical metric for evaluating membrane performance. We evaluated the specific energy consumption (SEC; kWh.m^{-3}) of the fabricated thin-film membrane together with the water recovery ratio (WRR_{sp})[65] in a single pass DCMD configuration (Fig. S22). This comprehensive metric, which accounts for both thermal (SEC_{the}) and electrical (SEC_{elec}) energy inputs required for the production of distilled water[66], includes energy for heating, cooling, and pumping, making it a reliable indicator of system efficiency (see detailed calculations in Supplementary Note 7)[67–74].

To validate energy savings under scalable conditions, we conducted strongly coupled multiscale CFD-membrane modeling, which revealed negligible temperature polarization at a feed temperature of 25 °C, enabling consistent operation across varying module lengths and flow rates (Fig. S23a). Under these ambient conditions, the TF0.1–1 membrane achieved a total SEC as low as 1.88 kWh.m^{-3} with a corresponding single-pass recovery (WRR_{sp}) of 0.32% (Fig. 4d and Supplementary Note 7.2). In this ambient operation, where the feed enters at room temperature without any heating (Fig. S22a), the maximum single-pass water recovery ratio is constrained by the first law of thermodynamics to 0.76% ($\Delta T = 5$ °C) (Supplementary Note 7.2). However, since MD is not significantly limited by increasing feed concentration, higher recoveries can be obtained under recirculating operation with auxiliary or waste-heat input using a heat exchanger.

When the feed temperature was increased to 35 °C, the SEC increased to 9.37 kWh.m^{-3} and WRR_{sp} rose to 1.12%. At 40 °C, the SEC reached 12.90 kWh.m^{-3} with a WRR_{sp} of 1.60%; at 50 °C SEC further increased to 16.65 kWh.m^{-3} and WRR_{sp} to 2.68 %; and at the highest feed temperature of 60 °C, SEC peaked at 20.65 kWh.m^{-3} with a WRR_{sp} of 3.87%. One can note the one order of magnitude increase in SEC as the temperature is increased from 25 °C to 35 °C, primarily attributed to the substantial thermal energy required to elevate the feed temperature, which intensifies with increasing operating temperatures.

At 60 °C, where the feed was preheated through a heat exchanger followed by external heating (Fig. S22b), the SEC increased more than tenfold compared to ambient operation, reflecting the substantially larger thermal input required and the stronger polarization effects (Fig. S23b). In this configuration, the maximum single-pass recovery is thermodynamically limited at 6.02%. Unlike the ambient case, where higher recoveries can be achieved through recirculation with low-grade heat input, operating at 60 °C inherently requires significant external thermal input, which sharply increases SEC. These findings emphasize the intrinsic advantage of the thin-film membrane in maintaining exceptionally low SEC under near-ambient operation, while providing a clear framework for distinguishing between ambient no-heating operation and high-temperature operation with external thermal input.

Given the membrane low SEC at ambient conditions, we further evaluated SEC across different feed compositions at 25 °C using both synthetic and real feed seawaters (Fig. 4d and Supplementary Note 7). The TF0.1–1 membrane consistently maintains low SEC values across all tested compositions, achieving 2.51 kWh.m^{-3} for 70 g.L^{-1} NaCl (WRR$_{sp}$ of 0.22%), 3.47 kWh.m^{-3} for real untreated seawater (WRR$_{sp}$ of 0.11%), and 4.43 kWh.m^{-3} for real SWRO brine (WRR$_{sp}$ of 0.09%) (Fig. 4d and Supplementary Note 7). Importantly, even when treating challenging high-salinity feeds like SWRO brine, conditions under which RO is generally impractical due to high osmotic pressures, the TF0.1–1 membrane sustains low SECs. The slightly higher SEC observed for real brine (compared to NaCl solutions) is likely due to reduced water flux at elevated salinities, caused by a lower vapor pressure and increased solution complexity. Moreover, the efficacy of MD as an evaporation-based desalination process is commonly assessed via its Gained Output Ratio (GOR). In this context, the fabricated thin film demonstrated an exceptional GOR of 21 (Supplementary Note 7). Additionally, an exergy analysis revealed a low exergy destruction (3.67 kWh.m^{-3}), two orders of magnitude lower than that of a commercial PTFE membrane (> 870 kWh.m^{-3}) when operated at the lowest temperature of 25 °C (see detailed analysis in Supplementary Note 9).

For such moderate feed temperatures, if a free heating resource (i.e., waste heat or solar energy) is available, the thermal energy required by the system becomes negligible, and the recovery ratio can be increased beyond the single-pass thermodynamic limit by employing recirculation or multi-effect operation. For example, the discharge (30–40 g.L^{-1}) from the dump condensers of thermal plants at 60 °C or brine discharge (60–70 g.L^{-1}) from thermal desalination processes at approximately 40 °C can be used as feed, significantly reducing the total SEC by offsetting heating demands. In such cases, only the energy needed for pumping or circulating water through the system remains (SEC$_{elec}$), which ranges between 0.1 and 0.4 kWh.m^{-3} for pilot-scale air gap MD[75] and 1.95 kWh.m^{-3} for a large-scale MD plant[76]. This low SEC is significantly lower than single-pass DCMD with heat recovery at a 60 °C feed temperature, which exhibits a minimum of 7.7 kWh.m^{-3} [77].

These results indicate that the fabricated thin films have a high potential for sustainable, energy-efficient desalination in the future. The energy requirements could be reduced to mere fluid recirculation if available heat sources are used, such as low-grade renewable sources (i.e., geothermal and solar energy sources), waste heat, or latent heat from rejected brine. Moreover, using multiple stages, where the latent heat of evaporation is recovered by heating up the inlet feed during vapor condensation in each stage, decreases the SEC value further and drives the system even closer to the thermodynamic limit of the process. This approach enables desalination at low SEC values (Fig. 4d) while maintaining sustainable productivity using a scalable, simple, and low-cost membrane. This performance is combined with the simplicity of the thin-film synthesis process, representing a breakthrough in desalination. This enhanced evaporation process can address water scarcity in arid lands, where solar energy or ambient temperature can be used to operate a system sustainably and obtain sufficient freshwater.

While the thin films demonstrated excellent SEC and desalination performance compared to commercial membranes, it is important to acknowledge that the current fabrication approach, based on a free-interface IP method, may incur higher production costs than those associated with conventional hydrophobic PTFE and SWRO membrane manufacturing. To address scalability and cost concerns, we propose adopting the in-situ IP (support-IP) method, which aligns with the established manufacturing processes used for polyamide (PA) layers in TFC-RO membranes, potentially reducing costs and facilitating large-scale production (see Supplementary Note 8). This method could take advantage of existing industrial infrastructure, enabling a more economical pathway for mass production. As illustrated in Figs. S24 and S25, the free-interface IP method produced a smoother and thinner nanofilm morphology than the support-IP method, likely due to the high heat capacity of water, which dissipates the exothermic heat generated during the IP reaction. In desalination tests (Fig. S26), a slight decrease in flux was observed for thin film fabricated using the support-IP process compared to those made by free-interface IP. Although additional optimization is necessary to ensure cost efficiency at both pilot and industrial scales, we believe this strategy holds promise for the broader economic feasibility of these membranes. Alongside cost and scalability considerations, it is crucial to carefully evaluate the environmental impact of the IP method. Although the large-scale fabrication of the membrane could leverage existing RO membrane manufacturing infrastructure, the conventional IP still involves organic solvents and potentially hazardous chemicals, posing sustainability and environmental safety concerns if not properly managed. Even though industrial-scale RO membrane manufacturing facilities currently adhere to stringent environmental and safety regulations, including solvent recovery systems and rigorous waste disposal protocols, there is an urgent need to pursue eco-friendly alternatives with the development of green solvents and new polymerization techniques aligned with global sustainability objectives.

Furthermore, while commercial PTFE membranes generally offer lower initial fabrication costs, they exhibit significant limitations in terms of productivity at lower operating temperatures, and low-temperature differences such as 5 °C, which restricts their energy efficiency. In contrast, our thin films retain high flux and thus low SEC at minimal temperature differences, offering a more sustainable solution with reduced energy demands. Although further work is required to fully optimize the scalability of this IP-based process, we believe that adopting an in-situ IP approach and aligning the production with TFC-RO infrastructure could significantly reduce costs and environmental impact while preserving the thin films' high desalination efficiency. This approach, alongside continued design optimization, could enhance the commercial viability of these membranes for sustainable desalination applications.

Discussion

Superhydrophobic thin films with subnanometer pores and submicron thickness were fabricated using a reaction between diamine and fluorine-based compounds. The thin films can desalinate highly challenging saline water, such as SWRO desalination brine with high performance and a very low energy consumption, achieving high energy efficiency for future sustainable desalination. The streamlined, scalable synthesis process, with potential cost reductions through in-situ IP, offers a promising pathway toward the commercial viability of these membranes for sustainable desalination. In future work, the desalination performance of a larger membrane area will be evaluated in a pilot-scale module.

Methods

Fabrication of polymeric thin films

For the synthesis of polymeric thin films, free-standing nanoporous hydrophobic polymeric thin films were initially fabricated using the IP technique. In a typical procedure, various amounts (Table S1) of 1H,1H,2H,2H-perfluorododecyltrichlorosilane (FTCS) were dissolved into 30 mL of hexane (Table S2). Similarly, an amount of m-phenylenediamine (MPD) were dissolved in deionized water to make 3 wt./vol. % of MPD/aqueous solution. Then, polymeric thin films were fabricated by carefully layering the hexane solutions FTCS onto the aqueous solution of MPD at room temperature (25 °C), for a selected time (see Table S1 for concentrations and reaction time details for the twelve thin films). Subsequently, the fabricated thin films were removed from the interface and transferred to water, where the low-density thin film remains floating on the surface. The TFC membranes were prepared by simply transferring the floating thins film onto the substrates, followed by curing at 120 °C for 3 min (Fig. 1 and Fig. S1).

Characterization

The surface and cross-sectional morphologies of the supported thin films were investigated using scanning electron microscopy (SEM, Nova Nano 630 and FEI Teneo VS). Atomic force microscopy (AFM, Dimension Icon SPM, model Dimension 3100, Veec) was used to measure the topography (2D and 3D) and roughness of the films. The wettability of the thin films was measured using a CAM 200 goniometer (KSV Instruments). Water contact angle (WCA) measurements were performed for at least 10 random positions, and the average value is reported in the results. An attenuated total reflectance Fourier-transform infrared (ATR-FTIR) spectrophotometer (PerkinElmer Spectrum 100S) was used to detect the functional groups present on the surface of the fabricated polymeric thin films. Raman spectroscopy (20-mW power) was used to demonstrate the binding properties of the thin films further. Raman signals were collected using a 473-nm laser system with 50× objective operated at a power of 20 mW. X-ray diffraction spectra (XRD) patterns were obtained using a Bruker D2 PHASER system with CuKα radiation ($\lambda = 1.54178$ Å), operating at 40 mA and 40 kV with a step of $0.02°\cdot s^{-1}$. Additional details are presented in Supplementary Note 2.

Desalination under ambient conditions

The desalination capabilities of the as-prepared thin films were evaluated at ambient conditions (25 °C) using a variety of saline solutions, including highly brackish water ($10\,g.L^{-1}$), seawater ($30\,g.L^{-1}$), brine ($70\,g.L^{-1}$), and solutions containing various salt ions ($MgCl_2$, KCl, and Na_2SO_4). Although most MD studies typically operate at higher transmembrane temperature differences, often utilizing feed temperatures around 60 °C and permeate temperatures around 20 °C (a 40 °C difference), we purposely selected a lower temperature difference of 5 °C. Indeed, while a larger temperature gradient generally enhances water flux, it also significantly increases energy demand, which remains a key obstacle to the broader adoption of MD. The prepared membrane demonstrates strong desalination performance under a minimal temperature gradient, thus offering a more energy-efficient alternative.

Desalination tests were conducted in a custom-designed experimental setup (Supplementary Note 4). The desalination performance of these polymeric thin film was quantified by measuring the water-vapor flux (J, $L.m^{-2}.h^{-1}$) and percentage of salt rejection (SR, %). Water-vapor flux was calculated by dividing the rate of change of the permeate mass by the active membrane area ($2\,cm^2$) and water density (Eq. (S1)). Salt rejection was calculated from the conductivity of the feed and permeate as presented in Eq. (S2). Each experiment was replicated at least three times to ensure reproducibility, and the average flux values were reported. All reported measurements were recorded only after the system had reached a stable operating condition.

In addition, the desalination performance of the thin films was tested using actual samples of seawater from the Red Sea and brine from a commercial seawater reverse osmosis (SWRO) plant, under ambient conditions (Table S6). The chlorine resistance of the thin films was evaluated by introducing 200 ppm of NaOCl to the feed side during the desalination process; stability and flux measurements were subsequently monitored over a period of three hours. Furthermore, the desalination capabilities under varying thin-film fabrication conditions, specifically the IP reaction time and reactant concentration, were examined. This aspect of the study involved nine different membranes, all assessed at room temperature (25 °C) for their ability to desalinate saline solutions. The performance of these membranes at varied feed temperatures was also investigated to determine the thermal effects on desalination efficiency. Further details can be found in the Supplementary Note 4.

Data availability

The data supporting the findings of this study are available within the article and its Supplementary Information files. All the raw data relevant to the study are available from the corresponding author upon request.

References

1. Zhang, W.-H. et al. Graphene oxide membranes with stable porous structure for ultrafast water transport. *Nat. Nanotechnol.* **16**, 337–343 (2021).
2. Karan, S., Jiang, Z. & Livingston, A. G. Sub–10 nm polyamide nanofilms with ultrafast solvent transport for molecular separation. *Science* **348**, 1347–1351 (2015).
3. Li, S. et al. Hydrophobic polyamide nanofilms provide rapid transport for crude oil separation. *Science* **377**, 1555–1561 (2022).
4. Jimenez-Solomon, M. F., Song, Q., Jelfs, K. E., Munoz-Ibanez, M. & Livingston, A. G. Polymer nanofilms with enhanced microporosity by interfacial polymerization. *Nat. Mater.* **15**, 760–767 (2016).
5. Gu, J. E. et al. Molecular layer-by-layer assembled thin-film composite membranes for water desalination. *Adv. Mater.* **25**, 4778–4782 (2013).
6. Chowdhury, M. R., Steffes, J., Huey, B. D. & McCutcheon, J. R. 3D printed polyamide membranes for desalination. *Science* **361**, 682–686 (2018).
7. Karan, S., Samitsu, S., Peng, X., Kurashima, K. & Ichinose, I. Ultrafast viscous permeation of organic solvents through diamond-like carbon nanosheets. *Science* **335**, 444–447 (2012).
8. Wittbecker, E. L. & Morgan, P. W. Interfacial polycondensation. I. *J. Polym. Sci.* **40**, 289–297 (1959).
9. Morgan, P. W. & Kwolek, S. L. Interfacial polycondensation. II. Fundamentals of polymer formation at liquid interfaces. *J. Polym. Sci.* **40**, 299–327 (1959).
10. Zhang, F., Fan, J. B. & Wang, S. Interfacial polymerization: from chemistry to functional materials. *Angew. Chem. Int. Ed.* **59**, 21840–21856 (2020).
11. Tan, Z., Chen, S., Peng, X., Zhang, L. & Gao, C. Polyamide membranes with nanoscale Turing structures for water purification. *Science* **360**, 518–521 (2018).
12. Cadotte, J. E., Petersen, R. J., Larson, R. E. & Erickson, E. E. A new thin-film composite seawater reverse osmosis membrane. *Desalination* **32**, 25–31 (1980).
13. Jin, X.-G. et al. Development of high permeability nanofiltration membranes through porous 2D MOF nanosheets. *Chem. Eng. J.*, 144566 (2023).
14. Shen, L. et al. Polyamide-based membranes with structural homogeneity for ultrafast molecular sieving. *Nat. Commun.* **13**, 500 (2022).
15. Zhu, C.-Y. et al. Polyamide nanofilms with linearly-tunable thickness for high performance nanofiltration. *J. Membr. Sci.* **627**, 119142 (2021).
16. Raaijmakers, M. J. & Benes, N. E. Current trends in interfacial polymerization chemistry. *Prog. Polym. Sci.* **63**, 86–142 (2016).

17. Song, Y., Fan, J.-B. & Wang, S. Recent progress in interfacial polymerization. *Mater. Chem. Front.* **1**, 1028–1040 (2017).
18. Thompson, K. A. et al. N-Aryl–linked spirocyclic polymers for membrane separations of complex hydrocarbon mixtures. *Science* **369**, 310–315 (2020).
19. Koh, D.-Y., McCool, B. A., Deckman, H. W. & Lively, R. P. Reverse osmosis molecular differentiation of organic liquids using carbon molecular sieve membranes. *Science* **353**, 804–807 (2016).
20. Trivedi, J. S., Bera, P., Bhalani, D. V. & Jewrajka, S. K. In situ amphiphilic modification of thin film composite membrane for application in aqueous and organic solvents. *J. Membr. Sci.* **626**, 119155 (2021).
21. Alduraiei, F., Kumar, S., Liu, J., Nunes, S. P. & Szekely, G. Rapid fabrication of fluorinated covalent organic polymer membranes for organic solvent nanofiltration. *J. Membr. Sci.* **648**, 120345 (2022).
22. Itoh, Y. et al. Ultrafast water permeation through nanochannels with a densely fluorous interior surface. *Science* **376**, 738–743 (2022).
23. Chen, X. et al. Ultrafast water evaporation through graphene membranes with subnanometer pores for desalination. *J. Membr. Sci.* **621**, 118934 (2021).
24. Chen, W. et al. High-flux water desalination with interfacial salt sieving effect in nanoporous carbon composite membranes. *Nat. Nanotechnol.* **13**, 345–350 (2018).
25. Zhao, S. et al. Hydrophilicity gradient in covalent organic frameworks for membrane distillation. *Nat. Mater.* **20**, 1551–1558 (2021).
26. Qtaishat, M. R. et al. Desalination at ambient temperature and pressure by a novel class of biporous anisotropic membrane. *Sci. Rep.* **12**, 13564 (2022).
27. Puranik, A. A., Rodrigues, L. N., Chau, J., Li, L. & Sirkar, K. K. Porous hydrophobic-hydrophilic composite membranes for direct contact membrane distillation. *J. Membr. Sci.* **591**, 117225 (2019).
28. Mitropoulos, A. C. The Kelvin equation. *J. Colloid Interface Sci.* **317**, 643–648 (2008).
29. Obaid, M. et al. Fabrication of highly permeable thin-film nanocomposite forward osmosis membranes via the design of novel freestanding robust nanofiber substrates. *J. Mater. Chem. A* **6**, 11700–11713 (2018).
30. Jiang, Z. et al. Aligned macrocycle pores in ultrathin films for accurate molecular sieving. *Nature* **609**, 58–64 (2022).
31. Chen, Y. et al. Rapid and precise molecular nanofiltration using ultra-thin-film membranes derived from 6,6′-Dihydroxy-2,2′-biphenyldiamine. *Adv. Funct. Mater.* **34**, 2406430 (2024).
32. Müller-Buschbaum, P. The active layer morphology of organic solar cells probed with grazing incidence scattering techniques. *Adv. Mater.* **26**, 7692–7709 (2014).
33. Fu, Q. et al. X-ray scattering studies of reverse osmosis materials. *Synchrotron Radiat. N.* **33**, 40–45 (2020).
34. Fu, Q. et al. Molecular Structure of Aromatic Reverse Osmosis Polyamide Barrier Layers. *ACS Macro Lett.* **8**, 352–356 (2019).
35. Fu, Q. Grazing Incidence Wide-Angle X-Ray Scattering Studies of Polyamide Thin-Film Selective Layers in Reverse Osmosis Membranes. State University of New York at Stony Brook (2021).
36. Ramesh, P. et al. A new class of "structure-by-design" polymer membranes for organic solvent nanofiltration with controllable selectivity. *J. Membr. Sci.* **692**, 122296 (2024).
37. Singh, P. S., Ray, P., Xie, Z. & Hoang, M. Synchrotron SAXS to probe cross-linked network of polyamide 'reverse osmosis' and 'nanofiltration' membranes. *J. Membr. Sci.* **421-422**, 51–59 (2012).
38. Tian, X. et al. Small and wide angle X-ray scattering to reveal nanoscale structure evolution of the polyamide RO membranes triggered by ethyl acetate. *J. Membr. Sci.* **693**, 122330 (2024).
39. Verploegen, E., Miller, C. E., Schmidt, K., Bao, Z. & Toney, M. F. Manipulating the Morphology of P3HT–PCBM Bulk Heterojunction Blends with Solvent Vapor Annealing. *Chem. Mater.* **24**, 3923–3931 (2012).
40. Socrates G. *Infrared and Raman characteristic group frequencies: tables and charts*. John Wiley & Sons (2004).
41. Shen, H., Wang, S., Xu, H., Zhou, Y. & Gao, C. Preparation of polyamide thin film nanocomposite membranes containing silica nanoparticles via an in-situ polymerization of SiCl4 in organic solution. *J. Membr. Sci.* **565**, 145–156 (2018).
42. Kozak, A. et al. Comparative investigation of Si-CN Films prepared by plasma enhanced chemical vapour deposition and magnetron sputtering. *Appl. Surf. Sci.* **425**, 646–653 (2017).
43. Afanasyev-Charkin, I. & Nastasi, M. Hard Si–N–C films with a tunable band gap produced by pulsed glow discharge deposition. *Surf. Coat. Technol.* **199**, 38–42 (2005).
44. Li, Y., Qi, S., Tian, M., Widjajanti, W. & Wang, R. Fabrication of aquaporin-based biomimetic membrane for seawater desalination. *Desalination* **467**, 103–112 (2019).
45. Alkhudhiri, A., Darwish, N. & Hilal, N. Treatment of high salinity solutions: Application of air gap membrane distillation. *Desalination* **287**, 55–60 (2012).
46. Alpatova, A., Alsaadi, A. & Ghaffour, N. Boron evaporation in thermally-driven seawater desalination: Effect of temperature and operating conditions. *J. Hazard. Mater.* **351**, 224–231 (2018).
47. Feng, S. & Xu, Z. Edges facilitate water evaporation through nanoporous graphene. *Nanotechnology* **30**, 165401 (2019).
48. Hummer, G., Rasaiah, J. C. & Noworyta, J. P. Water conduction through the hydrophobic channel of a carbon nanotube. *nature* **414**, 188–190 (2001).
49. Pascal, T. A., Goddard, W. A. & Jung, Y. Entropy and the driving force for the filling of carbon nanotubes with water. *Proc. Natl. Acad. Sci.* **108**, 11794–11798 (2011).
50. Giovambattista, N., Rossky, P. J. & Debenedetti, P. G. Effect of pressure on the phase behavior and structure of water confined between nanoscale hydrophobic and hydrophilic plates. *Phys. Rev. E* **73**, 041604 (2006).
51. Agrawal, K. V., Shimizu, S., Drahushuk, L. W., Kilcoyne, D. & Strano, M. S. Observation of extreme phase transition temperatures of water confined inside isolated carbon nanotubes. *Nat. Nanotechnol.* **12**, 267–273 (2017).
52. Otake, K. -i. et al. Confined water-mediated high proton conduction in hydrophobic channel of a synthetic nanotube. *Nat. Commun.* **11**, 1–7 (2020).
53. Beskok, A. & Karniadakis, G. Report: A Model For Flows in Channels, Pipes, and Ducts at Micro and Nano Scales. *Microscale Thermophysical Eng.* **3**, 43–77 (1999).
54. Klinkenberg, L. J. The Permeability of Porous Media to Liquids And Gases. In: *Drilling and Production Practice*). American Petroleum Institute (1941).
55. Civan, F. Effective Correlation of Apparent Gas Permeability in Tight Porous Media. *Transp. Porous Media* **82**, 375–384 (2010).
56. Florence, F. A., Rushing J., Newsham K. E. & Blasingame T. A. Improved Permeability Prediction Relations for Low Permeability Sands. In: *Rocky Mountain Oil & Gas Technology Symposium*). Society of Petroleum Engineers (2007).
57. Taghavinejad, A., Sharifi, M., Heidaryan, E., Liu, K. & Ostadhassan, M. Flow modeling in shale gas reservoirs: A comprehensive review. *J. Nat. Gas. Sci. Eng.* **83**, 103535 (2020).
58. Wu, K., Chen, Z., Li, X., Guo, C. & Wei, M. A model for multiple transport mechanisms through nanopores of shale gas reservoirs with real gas effect–adsorption-mechanic coupling. *Int. J. Heat. Mass Transf.* **93**, 408–426 (2016).
59. Soukane, S. & Ghaffour, N. Showerhead feed distribution for optimized performance of large scale membrane distillation modules. *J. Membr. Sci.* **618**, 118664 (2021).
60. Soukane, S., Lee, J.-G. & Ghaffour, N. Direct contact membrane distillation module scale-up calculations: Choosing between

convective and conjugate approaches. *Sep. Purif. Technol.* **209**, 279–292 (2019).

61. Zhong, J. et al. Exploring anomalous fluid behavior at the nanoscale: direct visualization and quantification via nanofluidic devices. *Acc. Chem. Res.* **53**, 347–357 (2020).
62. Kim, S., Kim, D., Kim, J., An, S. & Jhe, W. Direct evidence for curvature-dependent surface tension in capillary condensation: kelvin equation at molecular scale. *Phys. Rev. X* **8**, 041046 (2018).
63. Ding, Z., Ma, R. & Fane, A. G. A new model for mass transfer in direct contact membrane distillation. *Desalination* **151**, 217–227 (2003).
64. Lee, J., Laoui, T. & Karnik, R. Nanofluidic transport governed by the liquid/vapour interface. *Nat. Nanotechnol.* **9**, 317–323 (2014).
65. Lokare, O. R., Tavakkoli, S., Khanna, V. & Vidic, R. D. Importance of feed recirculation for the overall energy consumption in membrane distillation systems. *Desalination* **428**, 250–254 (2018).
66. Fattahi Juybari, H. et al. Unifying efficiency metrics for solar evaporation and thermal desalination. *ACS Energy Lett.* **9**, 4959–4975 (2024).
67. Blank, J., Tusel, G. & Nisanc, S. The real cost of desalted water and how to reduce it further. *Desalination* **205**, 298–311 (2007).
68. Al-Karaghouli, A. & Kazmerski, L. L. Energy consumption and water production cost of conventional and renewable-energy-powered desalination processes. *Renew. Sustain. Energy Rev.* **24**, 343–356 (2013).
69. Semiat, R. Energy issues in desalination processes. *Environ. Sci. Technol.* **42**, 8193–8201 (2008).
70. McGinnis, R. L., Hancock, N. T., Nowosielski-Slepowron, M. S. & McGurgan, G. D. Pilot demonstration of the NH3/CO2 forward osmosis desalination process on high salinity brines. *Desalination* **312**, 67–74 (2013).
71. Loganathan, K., Chelme-Ayala, P. & El-Din, M. G. Treatment of basal water using a hybrid electrodialysis reversal–reverse osmosis system combined with a low-temperature crystallizer for near-zero liquid discharge. *Desalination* **363**, 92–98 (2015).
72. Nassrullah, H., Anis, S. F., Hashaikeh, R. & Hilal, N. Energy for desalination: A state-of-the-art review. *Desalination* **491**, 114569 (2020).
73. Alawad, S. M. & Khalifa, A. E. Performance and energy evaluation of compact multistage air gap membrane distillation system: An experimental investigation. *Sep. Purif. Technol.* **268**, 118594 (2021).
74. Kim, J., Park, K., Yang, D. R. & Hong, S. A comprehensive review of energy consumption of seawater reverse osmosis desalination plants. *Appl. Energy* **254**, 113652 (2019).
75. Duong, H. C., Cooper, P., Nelemans, B., Cath, T. Y. & Nghiem, L. D. Evaluating energy consumption of air gap membrane distillation for seawater desalination at pilot scale level. *Sep. Purif. Technol.* **166**, 55–62 (2016).
76. Altmann, T., Robert, J., Bouma, A. & Swaminathan, J. Primary energy and exergy of desalination technologies in a power-water cogeneration scheme. *Appl. Energy* **252**, 113319 (2019).
77. Lin, S., Yip, N. Y. & Elimelech, M. Direct contact membrane distillation with heat recovery: Thermodynamic insights from module scale modeling. *J. Membr. Sci.* **453**, 498–515 (2014).

Acknowledgements

The research reported in this paper was supported by King Abdullah University of Science and Technology (KAUST), Saudi Arabia. The support from the Water Desalination and Reuse Platform (WDRP) staff is appreciated. Figure 1c (also used as the graphical abstract) was produced by Olga Kasimova, a scientific illustrator at KAUST. The authors are also grateful to KAUST Supercomputing Laboratory (KSL) for granting access to Shaheen III supercomputer through Project #k10047.

Author contributions

N.G. conceived the project, designed the experimental plan, and supervised all aspects of the work. M.O. fabricated the membranes and performed the characterization of the membranes and desalination experiments. S.S. developed the theoretical models, ran the simulations, and analyzed the modeling data. N.G., M.O., and S.S. jointly analyzed the experimental and simulation results. M.Q. and T.M. contributed to the discussion regarding the initial design of the membrane. V.G. analysis of the EDX data and contributed to the interpretation of the thin-film chemical structure, while M.A. performed the EDX measurements. Y.Z. conducted the GI-WAXS analysis, and V.S. performed the thermal conductivity measurement. H.O. M. and P.C. conducted the density and porosity measurements and analysis. G.M. and M.E. contributed to discussions on the chemistry and structure of the thin film. M.O. and S.S. drafted the manuscript. All authors contributed to revising the manuscript and approved the final version.

Competing interests

The authors declare no competing interests.

Additional information

Supplementary information The online version contains supplementary material available at https://doi.org/10.1038/s41467-025-68158-6.

Correspondence and requests for materials should be addressed to Noreddine Ghaffour.

Peer review information *Nature Communications* thanks Manish Kumar and the other, anonymous, reviewers for their contribution to the peer review of this work. A peer review file is available.